JOURNAL OF SYNCHROTRON RADIATION
ISSN 1600-5775

Atmospheric coherent X-ray diffraction imaging for *in situ* structural analysis at SPring-8 Hyogo beamline BL24XU

Yuki Takayama,[a,b]* Yuki Takami,[a] Keizo Fukuda,[a] Takamasa Miyagawa[a] and Yasushi Kagoshima[a]

[a]Graduate School of Material Science, University of Hyogo, 3-2-1 Kouto, Kamigori, Ako, Hyogo 678-1297, Japan, and [b]RIKEN SPring-8 Center, 1-1-1 Kouto, Sayo, Hyogo 679-5148, Japan.
*Correspondence e-mail: takayama@sci.u-hyogo.ac.jp

Received 17 November 2017
Accepted 26 April 2018

Edited by Y. Amemiya, University of Tokyo, Japan

Keywords: coherent X-ray diffraction imaging; non-crystalline samples; structural analysis; humidity control.

Coherent X-ray diffraction imaging (CXDI) is a promising technique for non-destructive structural analysis of micrometre-sized non-crystalline samples at nanometre resolutions. This article describes an atmospheric CXDI system developed at SPring-8 Hyogo beamline BL24XU for *in situ* structural analysis and designed for experiments at a photon energy of 8 keV. This relatively high X-ray energy enables experiments to be conducted under ambient atmospheric conditions, which is advantageous for the visualization of samples in native states. The illumination condition with pinhole-slit optics is optimized according to wave propagation calculations based on the Fresnel–Kirchhoff diffraction formula so that the sample is irradiated by X-rays with a plane wavefront and high photon flux of $\sim 1 \times 10^{10}$ photons/16 μm∅(FWHM)/s. This work demonstrates the imaging performance of the atmospheric CXDI system by visualizing internal voids of sub-micrometre-sized colloidal gold particles at a resolution of 29.1 nm. A CXDI experiment with a single macroporous silica particle under controlled humidity was also performed by installing a home-made humidity control device in the system. The *in situ* observation of changes in diffraction patterns according to humidity variation and reconstruction of projected electron-density maps at 5.2% RH (relative humidity) and 82.6% RH at resolutions of 133 and 217 nm, respectively, were accomplished.

1. Introduction

X-ray imaging and microscopic techniques play critical roles in non-destructive investigations of the structure–function relationships of both materials and biological samples (Liu *et al.*, 2016; Larabell & Nugent, 2010; Andrews *et al.*, 2011). In particular, the short wavelengths and high penetration depths of hard X-rays enable the seamless description of spatially hierarchical structures in samples from the millimetre to sub-micrometre scale by combining the available X-ray imaging techniques. Although the spatial resolutions of those X-ray imaging techniques are currently limited to several tens of nanometres because of difficulties in manufacturing the necessary X-ray optics and/or detector systems, the recent development of lensless coherent X-ray diffraction imaging (CXDI) techniques provides an opportunity to visualize the internal structures of samples from the micrometre to nanometre scale (Miao *et al.*, 2015). CXDI has thus far enabled non-destructive structural analysis of materials (Miao *et al.*, 2006; Barty *et al.*, 2008; Takahashi *et al.*, 2010; Jiang *et al.*, 2013) and biological samples (Kimura *et al.*, 2014; van der Schot *et al.*, 2015; Takayama *et al.*, 2015*b*; Rodriguez *et al.*, 2015) with

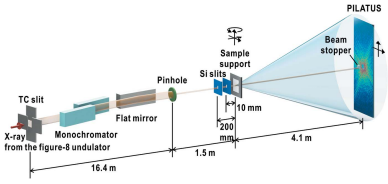

micrometre to sub-micrometre sizes at resolutions of tens of nanometres to several nanometres.

To achieve a deeper understanding of functional mechanisms, *in situ* imaging of functioning samples is also indispensable (Takano *et al.*, 2013; Weker *et al.*, 2014). The use of hard X-rays is advantageous for *in situ* experiments because the high transmission of hard X-rays enables experiments to be conducted under atmospheric conditions, which increases the flexibility of the sample environment. However, in many CXDI systems, all the components, including the samples, are placed in vacuum to detect weak diffraction signals from non-crystalline samples with adequate signal-to-noise ratio by reducing the X-ray attenuation and background scattering caused by air. The exposure of samples to vacuum also causes structural deformations in some cases. To keep samples in their native states, several special devices have been developed in the biological CXDI field (Lima *et al.*, 2009; Takayama & Nakasako, 2012; Nakasako *et al.*, 2013; Nam *et al.*, 2013; Kimura *et al.*, 2014; Kobayashi *et al.*, 2016*b*).

To enable *in situ* structural analysis of various samples in material and biological fields, we have developed an atmospheric CXDI system at SPring-8 Hyogo ID beamline BL24XU. The system is designed for sample imaging in an open-air environment. The pinhole illumination conditions are optimized according to the Fresnel–Kirchhoff diffraction formula in order to improve the photon flux and phase curvature at the sample. The performance of our system was demonstrated by applying it to colloidal gold particles. With this system, we performed a coherent diffraction experiment with a single macroporous silica particle under controlled humidity, which demonstrates the feasibility of future application to the *in situ* investigation of the structural responses of humidity-sensitive materials.

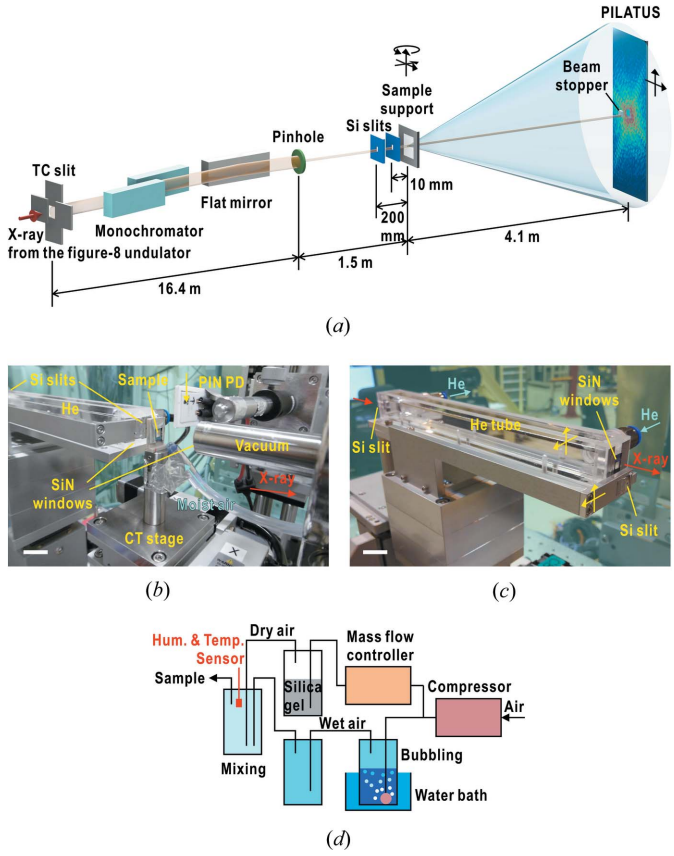

Figure 1
(*a*) Schematic illustration of the experimental setup. The flight tubes between the components are not shown. (*b*) Photographs showing the sample environment. The CT stage is composed of one vertical and two horizontal stages, a rotational stage along the vertical axis, and two horizontal stages on the rotational stage. (*c*) Photograph of the slit system. One of the silicon guard slits is attached to the upstream end of the helium tube. The downstream silicon slit in this photograph is moved out from the beam. (*d*) Schematic illustration of the home-made moist air generator. The scale bars in (*b*) and (*c*) indicate 10 mm.

2. Description of the atmospheric CXDI system at BL24XU

2.1. Overview of the system

The experimental setup of the atmospheric CXDI is shown in Fig. 1. This system was constructed at an imaging station of Hyogo ID beamline BL24XU at SPring-8 (Tsusaka *et al.*, 2001; Takano, 2009). To place samples in air, the system is optimized for experiments at a photon energy of 8 keV. Samples are mounted on an open-air computed tomography (CT) stage (Kohzu Precision Co. Ltd, Japan), which can tilt samples from −180 to +180° about the vertical axis (Fig. 1*b*). A home-made moist air generator can be optionally installed to control the relative humidity (RH) around the sample.

The pinhole, the slit system with two guard slits and the detector are also installed in the open, and flight tubes kept under vacuum are placed between them. To minimize the air path, one of the guard slits is directly attached to an acrylic tube filled with helium gas at atmospheric pressure which is mounted on an alignment stage (Fig. 1*c*). Open-air space of 38 mm along the beam is kept around the sample for installing devices for *in situ* imaging. Silicon nitride membranes with a thickness of 500 nm (Silson Ltd, UK) are used for the windows of the flight tubes to reduce background scattering, and a polyimide membrane is employed only for the window in front of the detector. Scattering from the last polyimide window is prevented by a beam stopper placed just before the window that blocks the direct beam.

2.2. Pinhole-slit optics and detector

A 30 µm-diameter tungsten pinhole (National Apertures Inc., USA) is used for the plane wave illumination. In CXDI, the flatness of the wavefront of the incident X-rays on the samples is critical for the phase retrieval calculations (Kohmura *et al.*, 2005). Thus, the pinhole-to-sample distance is determined according to the wave propagation calculation based on the Fresnel–Kirchhoff diffraction formula (Born & Wolf, 1999). Fig. 2 shows the intensity and phase distributions of diffracted wavefields 1.5 m (Fresnel region) and 3.0 m (near the Fraunhofer region) from the pinhole, which were calculated by assuming the pinhole to be illuminated by a uniform-

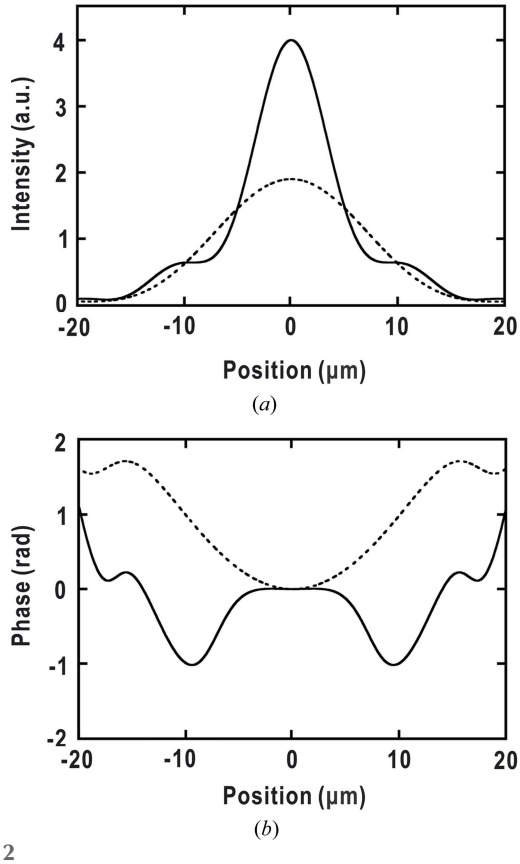

Figure 2
Calculated intensity and phase of diffracted waves from the pinhole. (*a*) Intensity and (*b*) phase distributions at 1.5 m (the Fresnel region) and 3.0 m (near the Fraunhofer region) downstream from the pinhole are shown with solid and dashed lines, respectively. Each phase distribution is plotted as a relative phase shift from the centre.

plane wave with a photon energy of 8 keV. We found the wavefront in the Fresnel region to be significantly flatter than that near the Fraunhofer region and the central intensity to be approximately twice as high as well. These features are advantageous for imaging micrometre-sized samples because they make the experiment less sensitive to positional drift of the samples and/or beam. Thus, we set the pinhole-to-sample distance to ∼1.5 m. For instance, the phase variation of the incident beam on a 3 μm sample was calculated to be less than $\pi/100$ rad within ∼3 μm from the beam centre in this setup.

Two square silicon apertures with sizes of 100 μm and 120 μm (Norcada Inc., Canada) are placed 200 mm and 10 mm upstream from the sample, respectively, as guard slits. Their edges are beveled at 35.3° against the beam. One corner of each slit is carefully adjusted to be as close to the incident beam as possible while monitoring the parasitic scattering using the PILATUS detector placed ∼4.1 m downstream from the sample. The direct beam and parasitic scattering passing through the apertures of the guard slits are blocked by the 3 mm × 3 mm tantalum beam stopper just before the detector. Using the PILATUS 100K (487 × 195 pixels, 172 μm per pixel; Dectris Ltd, Switzerland), diffraction patterns with spatial frequencies of up to 65.2 μm^{-1} can be recorded with a spatial frequency resolution of 0.27 μm^{-1} per pixel.

2.3. Humidity-control device

The system can optionally be equipped with a simple home-made humidity-control device (Fig. 1*d*), similar to that developed in protein crystallography (Takayama & Nakasako, 2011), to control the RH around the sample. Air with a maximum flow rate of 8 L min^{-1} from a compressor (AC0610A, NITTO KOHKI Co. Ltd, Japan) is divided into two paths, one of which flows into temperature-controlled water to generate vapour-saturated air by bubbling and the other is dried with silica gel. Then, the two components are mixed in a mixing bath, and the resultant moist air is blown toward the sample on the CT stage. The RH of the moist air is controlled by changing the mixing ratio of the air components with a mass flow controller (FCC-3000-G1, KOFLOC Co. Ltd, Japan). The RH and temperature of the moist air in the mixing bath are monitored with a sensor (SHT75, Sensirion AG, Switzerland). We confirmed in advance that the RH of the moist air surrounding the sample is almost the same as that in the mixing bath.

3. Experiments and data analysis

3.1. Sample preparation

Colloidal gold particles with a mean diameter of 400 nm (Sigma-Aldrich, USA) or macroporous silica particles with a mean diameter of 1.8 μm (M.S.Gel; AGC Si-Tech Co. Ltd, Japan) suspended in ethanol were dispersed on a silicon nitride membrane (Silson Ltd, UK) and then air-dried. The positions of the sample particles from one of the membrane corners were pre-measured using a scanning electron microscope (SEM; Miniscope TM3000, Hitachi High-Technologies Corporation, Japan) or digital microscope (HiROX Co. Ltd, Japan). Those coordinates were registered for sample identification upon exposure. The macroporous silica sample was kept in a desiccator at 20% RH to keep it dry until the diffraction experiment.

3.2. Atmospheric CXDI experiments

Horizontally polarized fundamental harmonics at 8 keV from a figure-8-type in-vacuum undulator (Tanaka & Kitamura, 1995) were extracted by a water-cooled horizontal dispersion silicon (111) double-crystal monochromator after passing through the transfer channel (TC) slit placed 49.26 m away from the source. The size of opening of the TC slit was adjusted to 100 μm (H) × 200 μm (W) to collimate the beam. Higher harmonics were eliminated by the rhodium-coated total-reflection plane mirror adjusted to an incident angle of 5.2 mrad. The atmospheric CXDI system described above was constructed so that the illumination pinhole was placed 16.4 m downstream from the TC slit. The position of the pinhole was carefully adjusted to extract a flat area of a single speckle originating from the mirror roughness.

The sample positions were refined around the registered sample position with coherent X-rays by monitoring the intensities and speckle visibilities of the diffraction patterns. The background patterns were collected at positions where no

speckles were observed. Because of the rectangular shape of the detector, three horizontal spatial frequency ranges (−69.0 to −16.9 μm^{-1}, −23.0 to 28.6 μm^{-1} and 16.9 to 69.0 μm^{-1}) were separately recorded for high-resolution imaging of the colloidal gold. On the other hand, the pixel size of the PILATUS was too large to oversample diffraction patterns from the silica particles. Thus, we collected 4 × 4 diffraction patterns shifted along both the horizontal and vertical directions in 1/4 pixel (43 μm step) steps and then applied the upsampling algorithm, as described below, in order to oversample the patterns sufficiently. This scheme reduced the effective pixel size to 43 μm.

3.3. Data processing and image reconstructions

After subtraction of the background intensity, the three partial diffraction patterns of the colloidal gold were patched to prepare a single high-resolution diffraction pattern. Similarly, an upsampled diffraction pattern of silica was prepared by applying the upsampling algorithm proposed by Chushkin & Zontone (2013) to the set of sub-pixel-shifted diffraction patterns. The consistency between the upsampled pattern and the sub-pixel-shifted data set was estimated with an $R_{\rm US}$-factor defined as

$$R_{\rm US} = \frac{1}{N^2}\sum_{i=1}^{N^2}\frac{\sum_{x',y'}\left|(1/N^2)\sum_{I(x,y)\in I_i(x',y')} I(x,y) - I_i(x',y')\right|}{\sum_{x',y'} I_i(x',y')}, \quad (1)$$

where $I(x, y)$ is the diffraction intensity of the upsampled diffraction pattern at an effective detector pixel (x, y), $I_i(x', y')$ is that of the ith observed sub-pixel-shifted pattern at the real detector pixel (x', y') and N is the number of shifts along each direction. $R_{\rm US}$ is just the average of the R-factors (Miao *et al.*, 2006) between the upsampled data and each sub-pixel-shifted intensity dataset. As demonstrated later, every diffraction pattern displayed good Friedel symmetry owing to the high photon energy of the X-rays used. Thus, the areas covered by the beam stopper were filled with Friedel pairs.

The projected electron-density maps were reconstructed from the diffraction patterns using software originally coded by Kodama & Nakasako (2011) and Oroguchi & Nakasako (2013) according to the modified protocol described by Takayama & Yonekura (2016). Briefly, both support estimation and phase refinement were performed by a combination of the hybrid-input–output phase-retrieval algorithm (Fienup, 1982) and the shrink-wrap shape-estimation algorithm (Marchesini *et al.*, 2003), followed by the error-reduction algorithm (Fienup, 1982) for better convergence. We conducted 500 independent reconstructions, and the 50 most probable reconstructions were selected by applying a principal component analysis (Sekiguchi *et al.*, 2016) combined with mean-shift clustering (Cheng, 1995). We produced the final projected electron-density map by averaging 50 reliable reconstructions. The effective resolution of the averaged map was determined as the inverse of the spatial frequency at which the phase-retrieval transfer function (PRTF; Chapman *et al.*, 2006) dropped below 0.5 (Sekiguchi *et al.*, 2016).

3.4. Water vapour adsorption isotherm measurement

The volume of water vapour adsorbed on the macroporous silica particles was measured by the constant-volume method using BELSORP18 (MicrotracBEL Corp., Japan). Prior to the measurement, a 130.2 mg sample was degassed for more than 12 h at 373 K under vacuum. The adsorbed volume of water vapour at 302 K was then measured automatically with an equilibration time of 500 s for each.

4. Results

4.1. Basic performance of the atmospheric CXDI system

Fig. 3 shows the beam profile at the sample (1.5 m from the pinhole) at 8 keV, measured using the knife-edge scan method with a thin gold wire as the knife-edge. The vertical profile closely agrees with the theoretical calculations, which indicates that the pinhole was irradiated with a nearly plane wave with high spatial coherence in the vertical direction. In contrast, the horizontal profile displays a wider unimodal shape. Although the low spatial coherence in the horizontal direction is an

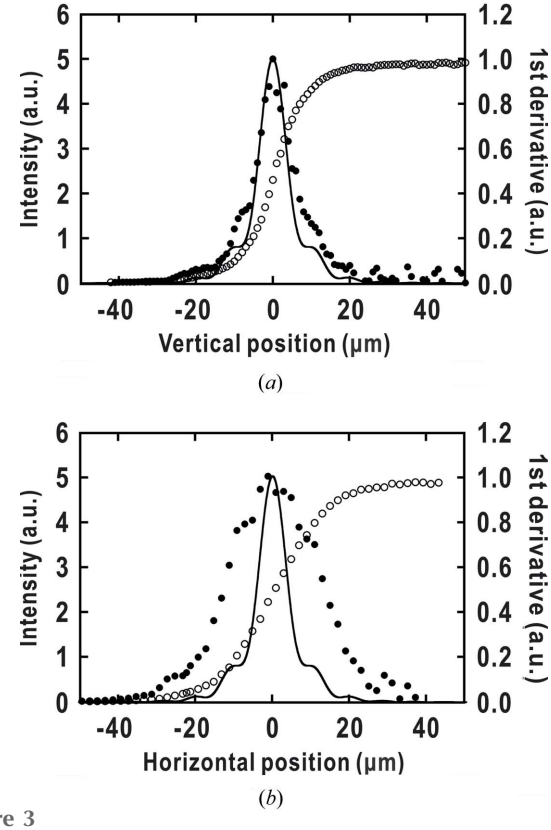

Figure 3
Measured intensity profiles of the incident beam at the sample position. The knife-edge scan intensity profiles (open circles) and their derivatives (filled circles) along the (*a*) vertical and (*b*) horizontal directions are shown. The solid line in each panel is the theoretical intensity profile calculated by using the Fresnel–Kirchhoff diffraction formula shown in Fig. 2.

intrinsic property of the synchrotron source, this deterioration of a coherent property can be partially caused by a residual heat load on the monochromator crystal (Kagoshima *et al.*, 2017). However, the spatial coherence at the sample is sufficient for the coherent illumination of a single isolated micrometre-sized sample, as demonstrated below.

Owing to the large pinhole diameter, the photon flux of the incident X-rays on the samples is as high as $\sim 1 \times 10^{10}$ photons / 16 µm ∅ (FWHM) / s at 8 keV. The throughput of the X-ray intensity from the pinhole to the detector was calculated to be 81%. The intensity loss is mainly a result of absorption by the polyimide window in front of the detector.

Table 1
Statistics of diffraction patterns and phase retrieval calculations.

		Macroporous silica	
Sample	Colloidal gold	At 5.2% RH	At 82.6% RH
Figure showing diffraction pattern	4(*b*)	6(*a*) left	6(*a*) right
Photon energy (keV)	8	10	10
Exposure time (min)	60	61	61
Application of the upsampling method	Not applied	Applied	Applied
R_{US}	–	0.15	0.27
Cross-correlation coefficient of Friedel pair, centre of the compared area (µm^{-1})	0.96, 12.5	0.96, 4.9	0.94, 4.9
Best resolution† (nm)	13	39	59
Reconstructed map in figure	4(*c*)	6(*b*) left	6(*b*) right
Resolution used for phase retrieval (nm)	14.6	74.7	74.7
Oversampling ratio‡	34.7	55.6	55.6
R_F§	0.27	0.25	0.33
Effective resolution¶ (nm)	29.1	132.8	217.4

† Inverse of a maximum spatial frequency where speckles could be observed. ‡ The oversampling ratio of the reconstructed map is defined as the number of pixels in the diffraction patterns divided by the number of pixels in a support of the map, which corresponds to the redundancy of the data (Miao *et al.*, 2003). § The definition of R_F is $R_F = \sum ||F_{obs}| - K|F_{calc}|| / \sum |F_{obs}|$, where $|F_{obs}|$ and $|F_{calc}|$ are the observed structural amplitude and that calculated from the averaged map, respectively, and K is a scale factor between the amplitudes (Miao *et al.*, 2006). K is calculated by using the linear least-squares method, but is ∼1. ¶ The effective full-period resolution of the averaged map is defined as the resolution at which the PRTF drops below 0.5 (Chapman *et al.*, 2006; Sekiguchi *et al.*, 2016).

4.2. Application to static CXDI under ambient atmospheric conditions

We performed high-resolution atmospheric CXDI on an assembly of colloidal gold particles (Fig. 4*a*) at a photon energy of 8 keV in order to demonstrate the imaging performance of the system. The patched diffraction pattern shown in Fig. 4(*b*) was recorded with an exposure time of 1 h for each part of the pattern. The pattern is composed of 8 × 9 pixel speckles with high visibility and displays good Friedel symmetry (Table 1). Speckles arranged in a cross-shape, which is characteristic of samples with rectangular projected densities, extend to the edge of the detector. We achieved a small-angle resolution of 1.1 µm^{-1} owing to the silicon guard slits with beveled edges, which yielded less parasitic scattering and worked well at 8 keV.

The projected electron density map was reconstructed at an effective full-period resolution of 29.1 nm (Figs. 4*c* and 4*d*, Table 1). The map is composed of one spherical and two cubic particles with sizes consistent with the mean size of the sample and two smaller particles. In the larger particles, 100–160 nm internal voids, which were not observable in the SEM image, could be resolved clearly. The observation of such voids is also difficult using transmission electron microscopy (Nakasako *et al.*, 2013).

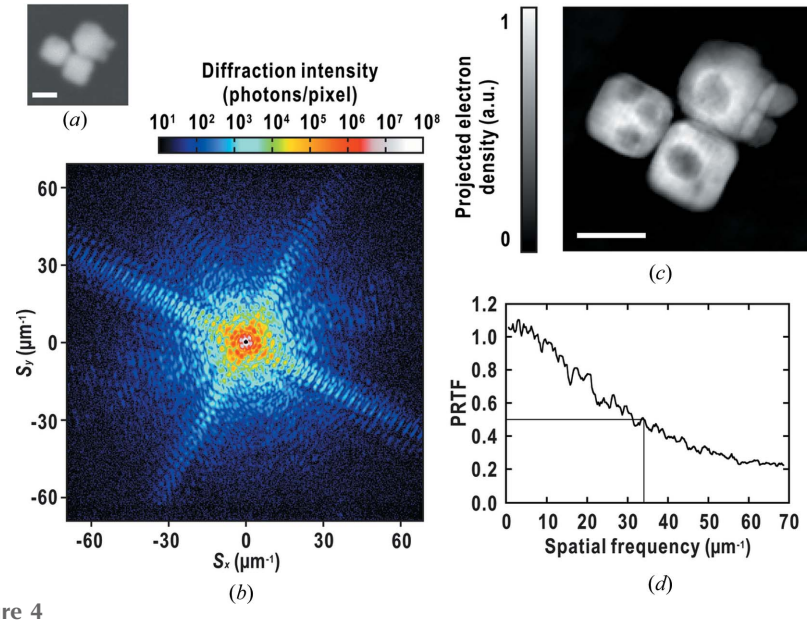

Figure 4
Visualization of internal voids in colloidal gold particles at 8 keV. (*a*) SEM image of the sample. (*b*) Diffraction pattern of the sample. (*c*) Projected electron density map reconstructed from the pattern in (*b*), where one pixel corresponds to 7.3 nm. (*d*) Phase retrieval transfer function of the map. The thin line indicates the spatial frequency corresponding to the effective resolution. The scale bars in (*a*) and (*c*) indicate 300 nm. The colour scales are shown at the top (*b*) and left (*c*) of each panel.

4.3. *In situ* observation of capillary condensation into the macroporous silica particle by humidity-controlled coherent X-ray diffraction

To investigate the feasibility of an *in situ* observation of the structural responses of humidity-sensitive materials, we attempted an *in situ* observation of capillary condensation into macropores of silica particles with a humidity-controlled coherent diffraction experiment. The sample silica particle (Fig. 5*a*) had a mean diameter of 1.8 µm and a nominal pore diameter of 100 nm. Fig. 5(*b*) shows a water-vapour adsorption isotherm of the

particles measured at 302 K by using the constant volume method (see §3.4). The curve, which displayed the typical shape for gas adsorption on macropores (Sing, 1985), indicates that the amount adsorbed increases and the response to humidity variation becomes sensitive at RH higher than ∼80%. Thus, we decided to conduct the CXDI of the particle at RH values of around 5%, 80% and 95%.

The CXDI experiment for the particle shown in Fig. 5(*a*) was performed at a photon energy of 10 keV with the experimental setup described above. This is because of the limitation of selectable photon energies under the dual-branch operation mode of BL24XU during the beam time. We increased the RH around the sample from 5 to 96% at around 302 K in a stepwise manner, as shown in Fig. 5(*c*), and collected diffraction patterns with an exposure time of 10 s. The estimated radiation dose was $\sim 3 \times 10^7$ Gy per pattern.

Fig. 5(*d*) shows diffraction patterns accumulated for 230 s at RHs of 5.2%, 82.6% and 95.6%. The peak-to-valley humidity variation during the exposures was less than 0.7% RH under a temperature variation of 0.1 K. Each pattern was not concentric, despite the spherical shape of the particle, but composed of many speckles, probably reflecting the porous structure of the particle. With increasing RH around the particle, an obvious change in the diffraction intensity distribution was observed at 95.6% RH (Fig. 5*d*). At this RH, the intensity of the speckles at high spatial frequencies significantly decreases, while that of the speckles at the low-spatial-frequency region up to ∼2.5 μm^{-1} increases. Such a change in diffraction patterns is expected when the density contrast between the silica body and pores is decreased (Kobayashi *et al.*, 2016*a*) by the capillary condensation, although similar changes may occur as a result of radiation damage.

To investigate the correlation of this diffraction intensity change with the humidity variation, we plotted the 'diffraction intensity ratio', defined as $\langle I(\mathbf{S})\rangle_{\mathbf{S}\in S_1}/\langle I(\mathbf{S})\rangle_{\mathbf{S}\in S_2}$ against the RH (Fig. 5*b*) and the elapsed time (Fig. 5*c*), where $\langle I(\mathbf{S})\rangle_{\mathbf{S}\in S}$ denotes the azimuthal average of diffraction intensities at a spatial frequency of S, and S_1 and S_2 were set to be 4.0 μm^{-1} and 7.4 μm^{-1}, respectively. This quantity is independent of the incident intensity fluctuation. As shown in Fig. 5(*c*), the variation of the diffraction intensity ratio appears to be well correlated with the RH variation. In addition, the variation of the intensity ratio to the RH variation showed a tendency similar to that of the water-vapour adsorption (Fig. 5*b*). These results suggest that the observed changes in the diffraction pattern were mainly a result of the response to the RH variation.

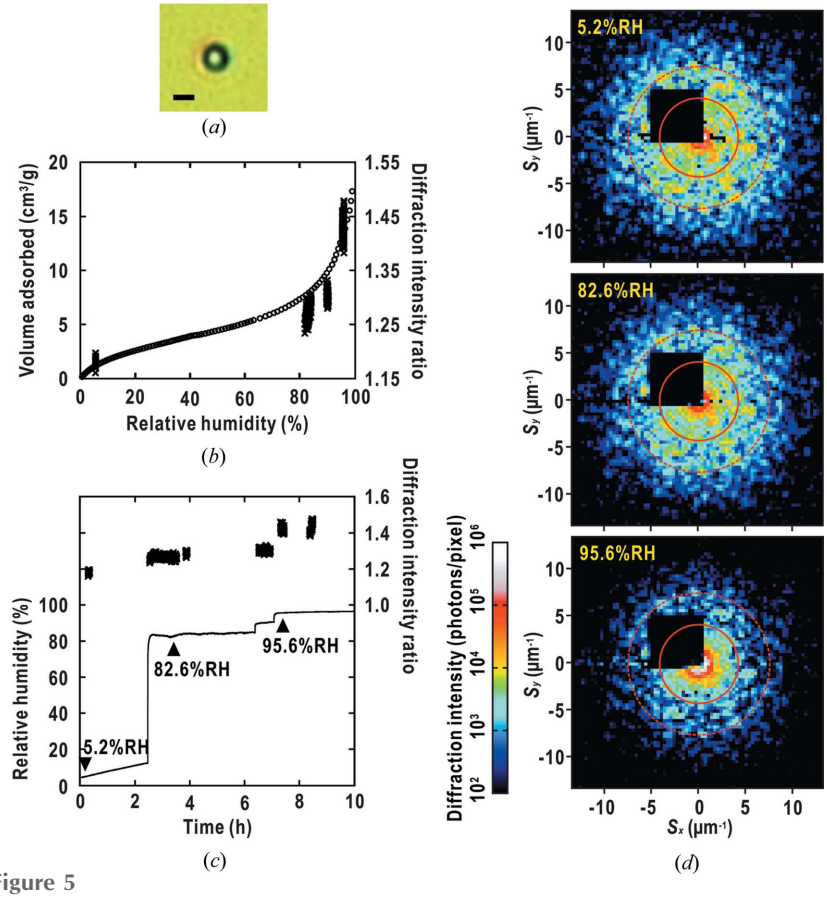

Figure 5
Coherent diffraction experiments performed on macroporous silica particles under controlled humidity. (*a*) Digital microscope image of the silica particle. (*b*) Water vapour adsorption isotherm of the particle, plotted with open circles. The diffraction-intensity ratio defined in the text is also plotted with cross symbols. (*c*) RH around the sample controlled by moist airflow (solid line). The diffraction intensity ratio is also plotted with cross symbols. (*d*) Coherent diffraction patterns of the single macroporous silica particle collected at the RHs indicated with arrowheads in (*c*). Non-upsampled patterns are shown. The red solid and broken circles indicate spatial frequencies of 4.0 μm^{-1} and 7.4 μm^{-1}, respectively. The black square area in each pattern is the shadow of the beam stopper. The colour scales are shown at the bottom left-hand corner. The scale bar in (*a*) indicates 1 μm.

4.4. Image reconstruction of macroporous silica with upsampling of diffraction patterns

Next, we tried to reconstruct the projected electron-density maps from the diffraction patterns shown in Fig. 5(*d*) to visualize structural responses. Because the practically required oversampling condition (Miao *et al.*, 2003) is not satisfied for the sample, we applied the upsampling method (Chushkin & Zontone, 2013). Fig. 6(*a*) shows the diffraction pattern of the silica particle at 5.2 and 82.6% RH after 4 × 4 upsampling. Each sub-pixel-shifted pattern was recorded with an exposure time of 230 s, resulting in a total exposure time of ∼61 min. We could not obtain the upsampled diffraction pattern at 95.6% RH, which is probably because of high-RH sensitivity and an excessively long exposure time as suggested from the values of $R_{\rm US}$ at 82.6% RH and 5.2% RH (Table 1), the values of which indicates consistency between the sub-pixel-shifted and the upsampled

patterns. The patterns display high visibility and good Friedel symmetry (Table 1), which indicates the reliability of the upsampling method. The upsampled patterns revealed that the diffraction intensity distributions at the low-spatial-frequency region up to $\sim$2.5 μm^{-1} were concentric, reflecting the spherical shape of the particle. The patterns at the higher-spatial-frequency region are composed of numerous speckles with $\sim$11 × 13 pixels. Unfortunately, the central crossed area on the patterns suffered from parasitic scattering attributed to the smaller absorption of 10 keV X-rays compared with 8 keV X-rays, and thus were omitted from the following phase retrieval calculations.

We successfully reconstructed projected electron-density maps of the particle at 5.2 and 82.6% RH at an effective full-period resolution of 133 and 217 nm, respectively (Figs. 6*b* and 6*c*, Table 1). The reconstruction from the non-upsampled diffraction pattern failed, probably because of the excessively small oversampling ratio (Table 1). The pore distribution is well resolved at 5.2% RH, especially at the periphery of the map, and consistent with that at 82.6% RH. The particle diameter and pore size are also consistent with the nominal size. These results demonstrate the reliability of the reconstructed maps. The pores in the map at 82.6% RH display lower contrast than those at 5.2% RH, but we could not conclude whether that was caused by the capillary condensation of the water vapour or a blurring effect that can be attributed to a worse spatial resolution at 82.6% RH.

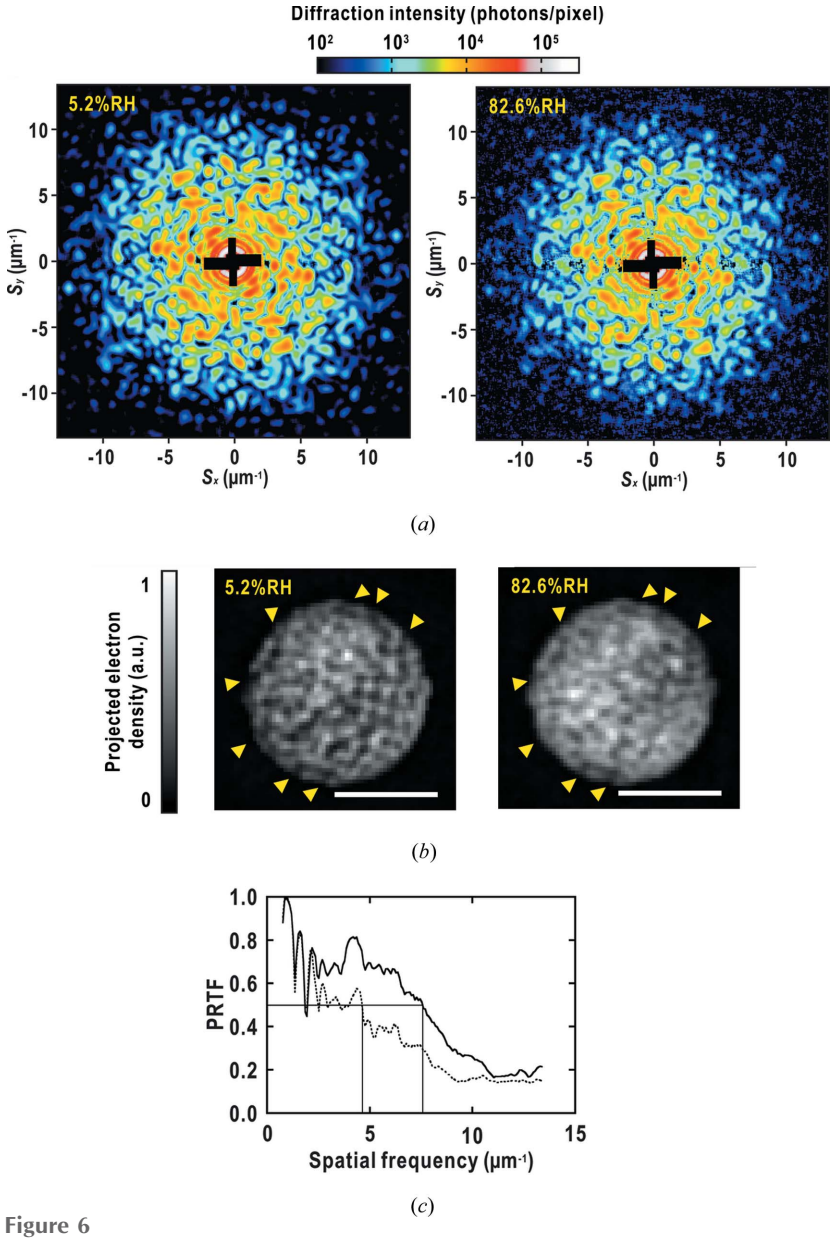

Figure 6
Image reconstruction of the macroporous silica particle at different RHs. (*a*) Upsampled diffraction patterns of the silica particle. The pattern was upsampled by 4 × 4, and then the Friedel average was applied. The central black-crossed areas were masked because of parasitic scatterings. (*b*) Projected electron density maps reconstructed from the patterns in (*a*). The opening of the pores at the periphery of the map are indicated by arrowheads. One pixel corresponds to 37.4 nm. (*c*) Phase retrieval transfer function of the maps at 5.2% RH (solid line) and 82.6% RH (broken line). The thin lines indicate the spatial frequencies corresponding to the effective resolution. The scale bars in (*b*) indicate 1 μm. The colour scales are shown at the top (*a*) and left (*b*) of each panel.

5. Discussions

We developed an atmospheric CXDI system at Hyogo ID beamline BL24XU at SPring-8. The good imaging performance of the system was demonstrated by application to colloidal gold particles. We also demonstrated the *in situ* structural investigation of the macroporous silica particle by CXDI under controlled humidity. Although the spatial resolutions were limited, the results demonstrate the potential for humidity-controlled CXDI in the structural analysis of humidity-sensitive materials. Here we discuss the feasibility of future *in situ* structural analysis with the atmospheric CXDI system.

5.1. Performance of the atmospheric CXDI system

In our system, the samples were placed before the Fraunhofer region of X-rays diffracted by the pinhole. The vertical intensity profile (Fig. 3*a*) showed good agreement with the theoretical case, which indicates that the spatial coherence along the vertical direction was nearly ideal even after the beamline optics such as the monochromator and the mirror. The successful reconstruction of the high-resolution projected map (Fig. 4 and Table 1) also demonstrates that the plane-wave illumination conditions required for CXDI (Kohmura *et al.*, 2005) were satisfied at least for the sizes of the samples used in the present study. The coherence property, especially for the horizontal direction, may be improved by

upgrading the monochromator to a liquid-nitrogen-cooled type, scheduled in 2018.

In CXDI, the upper sample size limit is determined by the oversampling condition, which depends on sample sizes, detector pixel size and the sample-to-detector distance, as well as the spatial coherence length of the beam at the sample position. In the current setup, samples smaller than ∼1.6 µm at 8 keV and ∼1.3 µm at 10 keV will satisfy the oversampling condition recommended for phase retrieval from experimental data, *i.e.* a factor of five (Miao *et al.*, 2003). The upsampling method implemented in the present study is an effective means of overcoming the sample-size limitation, as demonstrated in §4.4. According to a simulation performed to investigate the noise tolerance of the upsampling algorithm, the algorithm will not significantly deteriorate the signal-to-noise ratios of diffraction patterns (Takayama *et al.*, in preparation), but inconsistency in the sub-pixel-shifted dataset will deteriorate upsampling reconstructions. The results shown in Fig. 6 indicate that the stability of the system regarding the drift of the incident beam and/or samples is sufficient for the upsampling measurements. However, the macroporous silica particle was too sensitive to the RH fluctuations to apply the upsampling method, especially at high RH. Slowing the response by coating samples with a thin layer of oils or polymer glues (Kiefersauer *et al.*, 2000; Baba *et al.*, 2013) may be effective.

5.2. Feasibility of future *in situ* imaging by the atmospheric CXDI

In our humidity-controlled CXDI, we concluded that the observed structural changes in the macroporous silica were mainly caused by the RH variation around the sample. On the other hand, radiation damage may also cause structural changes, and thus, the dose limit for samples is one of the big obstacles for the practical application of *in situ* CXDI. In future *in situ* CXDI experiments, it may not be possible to collect a complete tomographic dataset because of factors such as radiation damage (Howells *et al.*, 2009), temporal resolution limitations and geometrical restrictions imposed by the environmental control devices. In such situations, depth analysis based on stereo matching (Hartley & Zisserman, 2004) may be beneficial for deriving semi-quantitative three-dimensional structural information (Hoshino *et al.*, 2011). In addition, methods for enhancing the diffraction signals by utilizing strong scatterers (Kim *et al.*, 2014; Takayama *et al.*, 2015*a*; Takayama & Yonekura, 2016) may improve the spatial and/or temporal resolutions within the tolerable dose range. An increase in coherent flux provided by diffraction-limited storage rings (Eriksson *et al.*, 2014; Yabashi *et al.*, 2014) will offer opportunities for *in situ* imaging with high temporal resolutions as well.

The ability of mounting samples in air without an enclosing chamber is beneficial for future *in situ* CXDI because there are fewer limitations in terms of environmental control devices. The devices can be exchanged easily according to the physical properties to be investigated. Here, we presented the results of CXDI under controlled humidity (Figs. 5 and 6). Lima *et al.* (2009) also introduced a cryogenic nitrogen gas jet device used in protein crystallography for measurements under cryogenic temperatures. We believe that our atmospheric CXDI system will extend the possibility of *in situ* structural studies in both the material and biological fields.

Acknowledgements

We are grateful to Professor Masayoshi Nakasako at Keio University and Professor Masaki Yamamoto at RIKEN for their stimulating discussions and for providing silicon guard slits. We again appreciate Professor Masayoshi Nakasako for generously providing the original software for phase retrieval. We also thank Dr Yoshimasa Urushihara, Ms Haruka Yamada and Ms Rumi Suzuki at the University of Hyogo for their assistance with the CXDI experiments. The macroporous silica sample was generously provided by AGC Si-Tech Co. Ltd. The water-vapour adsorption isotherm was measured by U. B. E. Scientific Analysis Lab. Ltd. We greatly appreciate the referees' comments and suggestions for improving the manuscript. We would like to thank Editage for English language editing.

Funding information

The following funding is acknowledged: University of Hyogo (a special grant for research to Yuki Takayama). The CXDI experiments were performed at BL24XU of SPring-8 with approval from the Japan Radiation Research Institute (proposal Nos. 2016A3200, 2016B3201).

References

Andrews, J. C., Meirer, F., Liu, Y., Mester, Z. & Pianetta, P. (2011). *Microsc. Res. Tech.* **74**, 671–681.
Baba, S., Hoshino, T., Ito, L. & Kumasaka, T. (2013). *Acta Cryst.* D**69**, 1839–1849.
Barty, A., Marchesini, S., Chapman, H. N., Cui, C., Howells, M. R., Shapiro, D. A., Minor, A. M., Spence, J. C. H., Weierstall, U., Ilavsky, J., Noy, A., Hau-Riege, S. P., Artyukhin, A. B., Baumann, T., Willey, T., Stolken, J., van Buuren, T. & Kinney, J. H. (2008). *Phys. Rev. Lett.* **101**, 055501.
Born, M. & Wolf, E. (1999). *Principles of Optics*, 7th ed. Cambridge University Press.
Chapman, H. N., Barty, A., Marchesini, S., Noy, A., Hau-Riege, S. P., Cui, C., Howells, M. R., Rosen, R., He, H., Spence, J. C. H., Weierstall, U., Beetz, T., Jacobsen, C. & Shapiro, D. (2006). *J. Opt. Soc. Am. A*, **23**, 1179–1200.
Cheng, Y. (1995). *IEEE Trans. Pattern Anal. Mach. Intell.* **17**, 790–799.
Chushkin, Y. & Zontone, F. (2013). *J. Appl. Cryst.* **46**, 319–323.
Eriksson, M., van der Veen, J. F. & Quitmann, C. (2014). *J. Synchrotron Rad.* **21**, 837–842.
Fienup, J. R. (1982). *Appl. Opt.* **21**, 2758–2769.
Hartley, R. & Zisserman, A. (2004). *Multiple View Geometry in Computer Vision*. Cambridge University Press.
Hoshino, M., Uesugi, K., Pearson, J., Sonobe, T., Shirai, M. & Yagi, N. (2011). *J. Synchrotron Rad.* **18**, 569–574.
Howells, M. R., Beetz, T., Chapman, H. N., Cui, C., Holton, J. M., Jacobsen, C. J., Kirz, J., Lima, E., Marchesini, S., Miao, H., Sayre, D., Shapiro, D. A., Spence, J. C. H. & Starodub, D. (2009). *J. Electron Spectrosc. Relat. Phenom.* **170**, 4–12.

Jiang, H., Xu, R., Chen, C.-C., Yang, W., Fan, J., Tao, X., Song, C., Kohmura, Y., Xiao, T., Wang, Y., Fei, Y., Ishikawa, T., Mao, W. L. & Miao, J. (2013). *Phys. Rev. Lett.* **110**, 205501.
Kagoshima, Y., Miyagawa, T., Kagawa, S., Takeda, S. & Takano, H. (2017). *Rev. Sci. Instrum.* **88**, 086110.
Kiefersauer, R., Than, M. E., Dobbek, H., Gremer, L., Melero, M., Strobl, S., Dias, J. M., Soulimane, T. & Huber, R. (2000). *J. Appl. Cryst.* **33**, 1223–1230.
Kim, C., Kim, Y., Song, C., Kim, S. S., Kim, S., Kang, H. C., Hwu, Y., Tsuei, K.-D., Liang, K. S., Noh, D. Y. & do, Y. (2014). *Opt. Express*, **22**, 29161–29169.
Kimura, T., Joti, Y., Shibuya, A., Song, C., Kim, S., Tono, K., Yabashi, M., Tamakoshi, M., Moriya, T., Oshima, T., Ishikawa, T., Bessho, Y. & Nishino, Y. (2014). *Nat. Commun.* **5**, 3052.
Kobayashi, A., Sekiguchi, Y., Oroguchi, T., Okajima, K., Fukuda, A., Oide, M., Yamamoto, M. & Nakasako, M. (2016*a*). *J. Synchrotron Rad.* **23**, 975–989.
Kobayashi, A., Sekiguchi, Y., Takayama, Y., Oroguchi, T., Shirahama, K., Torizuka, Y., Manoda, M., Nakasako, M. & Yamamoto, M. (2016*b*). *Rev. Sci. Instrum.* **87**, 053109.
Kodama, W. & Nakasako, M. (2011). *Phys. Rev. E*, **84**, 021902.
Kohmura, Y., Nishino, Y., Ishikawa, T. & Miao, J. (2005). *J. Appl. Phys.* **98**, 123105.
Larabell, C. A. & Nugent, K. A. (2010). *Curr. Opin. Struct. Biol.* **20**, 623–631.
Lima, E., Wiegart, L., Pernot, P., Howells, M., Timmins, J., Zontone, F. & Madsen, A. (2009). *Phys. Rev. Lett.* **103**, 198102.
Liu, Y., Kiss, A. M., Larsson, D. H., Yang, F. & Pianetta, P. (2016). *At. Spectrosc.* **117**, 29–41.
Marchesini, S., He, H., Chapman, H. N., Hau-Riege, S. P., Noy, A., Howells, M. R., Weierstall, U. & Spence, J. C. H. (2003). *Phys. Rev. B*, **68**, 140101.
Miao, J., Chen, C.-C., Song, C., Nishino, Y., Kohmura, Y., Ishikawa, T., Ramunno-Johnson, D., Lee, T.-K. & Risbud, S. H. (2006). *Phys. Rev. Lett.* **97**, 215503.
Miao, J., Ishikawa, T., Anderson, E. H. & Hodgson, K. O. (2003). *Phys. Rev. B*, **67**, 174104.
Miao, J., Ishikawa, T., Robinson, I. K. & Murnane, M. M. (2015). *Science*, **348**, 530–535.
Nakasako, M., Takayama, Y., Oroguchi, T., Sekiguchi, Y., Kobayashi, A., Shirahama, K., Yamamoto, M., Hikima, T., Yonekura, K., Maki-Yonekura, S., Kohmura, Y., Inubushi, Y., Takahashi, Y., Suzuki, A., Matsunaga, S., Inui, Y., Tono, K., Kameshima, T., Joti, Y. & Hoshi, T. (2013). *Rev. Sci. Instrum.* **84**, 093705.
Nam, D., Park, J., Gallagher-Jones, M., Kim, S., Kim, S., Kohmura, Y., Naitow, H., Kunishima, N., Yoshida, T., Ishikawa, T. & Song, C. (2013). *Phys. Rev. Lett.* **110**, 098103.
Oroguchi, T. & Nakasako, M. (2013). *Phys. Rev. E*, **87**, 022712.
Rodriguez, J. A., Xu, R., Chen, C.-C., Huang, Z., Jiang, H., Chen, A. L., Raines, K. S., Pryor, A. Jr, Nam, D., Wiegart, L., Song, C., Madsen, A., Chushkin, Y., Zontone, F., Bradley, P. J. & Miao, J. (2015). *IUCrJ*, **2**, 575–583.
Schot, G. van der, Svenda, M., Maia, F. R. N. C., Hantke, M., DePonte, D. P., Seibert, M. M., Aquila, A., Schulz, J., Kirian, R., Liang, M., Stellato, F., Iwan, B., Andreasson, J., Timneanu, N., Westphal, D., Almeida, F. N., Odic, D., Hasse, D., Carlsson, G. H., Larsson, D. S. D., Barty, A., Martin, A. V., Schorb, S., Bostedt, C., Bozek, J. D., Rolles, D., Rudenko, A., Epp, S., Foucar, L., Rudek, B., Hartmann, R., Kimmel, N., Holl, P., Englert, L., Duane Loh, N., Chapman, H. N., Andersson, I., Hajdu, J. & Ekeberg, T. (2015). *Nat. Commun.* **6**, 5704.
Sekiguchi, Y., Oroguchi, T. & Nakasako, M. (2016). *J. Synchrotron Rad.* **23**, 312–323.
Sing, K. S. W. (1985). *Pure Appl. Chem.* **57**, 603–619.
Takahashi, Y., Nishino, Y., Tsutsumi, R., Zettsu, N., Matsubara, E., Yamauchi, K. & Ishikawa, T. (2010). *Phys. Rev. B*, **82**, 214102.
Takano, H. (2009). *SPring-8 Research Frontiers 2008*, 190.
Takano, H., Morikawa, M., Konishi, S., Azuma, H., Shimomura, S., Tsusaka, Y., Nakano, S., Kosaka, N., Yamamoto, K. & Kagoshima, Y. (2013). *J. Phys. Conf. Ser.* **463**, 012025.
Takayama, Y., Inui, Y., Sekiguchi, Y., Kobayashi, A., Oroguchi, T., Yamamoto, M., Matsunaga, S. & Nakasako, M. (2015*b*). *Plant Cell Physiol.* **56**, 1272–1286.
Takayama, Y., Maki-Yonekura, S., Oroguchi, T., Nakasako, M. & Yonekura, K. (2015*a*). *Sci. Rep.* **5**, 8074.
Takayama, Y. & Nakasako, M. (2011). *Biophys. Chem.* **159**, 237–246.
Takayama, Y. & Nakasako, M. (2012). *Rev. Sci. Instrum.* **83**, 054301.
Takayama, Y. & Yonekura, K. (2016). *Acta Cryst.* A**72**, 179–189.
Tanaka, T. & Kitamura, H. (1995). *Nucl. Instrum. Methods Phys. Res. A*, **364**, 368–373.
Tsusaka, Y., Yokoyama, K., Takeda, S., Takai, K., Kagoshima, Y. & Matsui, J. (2001). *Nucl. Instrum. Methods Phys. Res. A*, **467–468**, 670–673.
Weker, J. N., Liu, N., Misra, S., Andrews, J. C., Cui, Y. & Toney, M. F. (2014). *Energ. Environ. Sci.* **7**, 2771–2777.
Yabashi, M., Tono, K., Mimura, H., Matsuyama, S., Yamauchi, K., Tanaka, T., Tanaka, H., Tamasaku, K., Ohashi, H., Goto, S. & Ishikawa, T. (2014). *J. Synchrotron Rad.* **21**, 976–985.